MOF Derived Porous ZnO/C Nanocomposites for Efficient Dye Photodegradation

Mian Zahid Hussain,[a, b] Andreas Schneemann,[b, c] Roland A. Fischer,[b] Yanqiu Zhu,[a] and Yongde Xia[*, a]

[a] College of Engineering, Mathematics and Physical Sciences, University of Exeter, Exeter EX4 4QF, U. K.

[b] Catalysis Research Center, Department of Chemistry, Technical University of Munich, Ernst-OttO-Fischer-straße 1, 85748 Garching, Germany.

Corresponding author: Y.Xia@exeter.ac.uk; Tel: +44 1392 723683

ABSTRACT

Homogeneously dispersed crystalline ZnO nanoparticles embedded in porous carbon matrix were synthesized via a one-step carbonization of porous metal-organic framework MOF-5 at 800 °C and 1000 °C in different gas atmospheres. The resulting ZnO/C nanocomposites generally retain cubic particle morphology and high specific surface area of the precursor MOF-5. Various characterization techniques, including XRD, SEM, TEM, elemental mapping, Raman, FTIR and XPS, confirmed that the carbonization of MOF-5 in water vapor atmosphere produced homogeneously dispersed ZnO nanoparticles confined within the functionalized porous carbon matrix. The rich oxygen-containing hydrophilic functional groups on the surface of the nanocomposite, the defects in the carbon doped ZnO nanostructure, the crystalline ZnO nanoparticles and the high textural properties resulted in excellent methylene blue adsorption and photodegradation performance under visible light irradiation. This simple and environmentally friendly approach can be further employed to harvest a variety of new homogeneously dispersed functional metal oxide/carbon composites for various environment and energy related applications.

1. INTRODUCTION

Due to the high industrialization, fresh water sources and eventually the oceans are polluted every day. Big industries produce a variety of hazardous contaminants, such as organic chemical wastes, byproducts from textile dyes, petrochemicals, pesticides and plastics etc. The treatment of industrial wastewater has become one of the major challenges in our society. There have been enormous efforts to utilize metal oxide as photocatalysts to decompose organic pollutants in wastewater into environmentally benign species.[1] Zinc oxide (ZnO) is an excellent semiconductor material for this purpose because of its nontoxicity and abundance.[2, 3] However, the wide energy band gap of ZnO hinders its utilization in the visible light range of the electromagnetic spectrum since bulk ZnO can only absorbs UV light with wavelength shorter than 380 nm, which consequently restricts the photocatalytic efficiency.[4] Furthermore, the low surface area of ZnO and its tendency to agglomerate due to high surface energies are big challenges to effectively utilize ZnO nanoparticles for photocatalysis.[5, 6]

To overcome these limitations, plenty of approaches were developed to generate ZnO-based composites so that the band gap and therefore the photocatalytic performance of the materials can be tuned.[7] However, the composites synthesized by mechanical and physical methods usually possess low surface area, poor dispersion and heterogeneity.[7] In the past several years, carbonization of MOFs precursors has drawn huge attention due to the tunable properties of the resulting materials.[8] Actually, metal-organic frameworks (MOFs) have been proved to be very promising sacrificial templates to generate ZnO nanaoparticles embedded in porous carbon frameworks with high specific surface areas, tunable pore sizes, increased thermal stability and homogeneously dispersed crystalline ZnO nanoparticles.[9] Simultaneously, during the high temperature heat treatment of MOFs, the formed carbon derived from the carbonization of organic linkers also diffuses into the crystal lattice of ZnO which can adjust the energy band gap of ZnO.[10] Consequently, it may result in high performance materials for photocatalytic applications.

MOFs are porous crystalline structures, consisting of metal containing vertices interconnected by organic struts.[11-13] In Zn-based MOF-5, the Zn_4O metal cluster is connected to six carboxylates, constructing octahedral-shaped building units linked through rod-like organic BDC^{2-}(1,4-benzenedicarboxylate) linkers to form a cubic structure with the composition

$Zn_4O(BDC)_3$.[14] Due to their permanent high porosity, structural flexibility and wide functionalities, MOFs are considered as ideal candidates for applications in gas separation,[15] sensors,[16] biomedicine,[17] super-capacitors[18], Li-ion batteries[19] and catalysis.[20-21] However, the direct employment of MOF-5 in photocatalytic wastewater treatment has not been promising due to the structural instability upon moisture exposure.[22] To retain the inherent structures, porosity and surface functionalities of MOF-5, one step pyrolysis of MOF-5 was carried out to derive the ZnO/C nanocomposites.

The adsorption and photocatalytic degradation of organic dyes depends on several parameters, including the surface charges, surface functionalization, hydrophilic/hydrophobic nature and textural properties of the products.[9] The open pore networks can facilitate the diffusion of organic dye molecules to access the pore surface lined with ZnO photocatalysts. Upon visible light irradiation, electron-hole pairs are generated in semiconducting ZnO/C nanocomposites. The generated electrons transfer to the conduction band and produce superoxides (O_2^-) and the holes in valance band form hydroxyl ($\cdot OH$) radicals via water oxidation. The reduction of organic dye is induced by superoxides, whereas the $\cdot OH$ radicals oxidize the organic dye leading to its complete decoloration and finally mineralization.[1, 23-25]

A few reports on MOF derived ZnO/C nanocomposites for photocatalytic water treatment have been published.[26] However, many questions remain unanswered. For instance, the interactions of the nanocomposites with organic dyes and the impact of defects and functional groups on photocatalytic activity have not been thoroughly studied. In 2011, Park *et al.* prepared ZnO/C hybrids by direct carbonization of MOF-5 at 600 °C in N_2 atmosphere and the resulting ZnO/C composite showed photocatalytic Rhodamine B degradation under UV irradiation.[26] Recently, we exploited the use of water steam atmosphere to synthesize ZnO/N-doped nanoporous carbon composites from zeolitic imidazolate framework ZIF-8 ($Zn(mIm)_2$; where mIm is 2-methylimidazole) at 800 °C for CO_2 uptake and organic pollutant methylene blue (MB) removal from water.[27]

In this contribution, the effect of temperatures and the gaseous atmospheres during the carbonization process on the compositions, the morphologies and properties of the resulting ZnO/C nanocomposites have been studied. Though there are a few studies available on MOF derived ZnO/C composites for photocatalysis, to the best of our knowledge, no detailed study is

available on the effect of gaseous atmosphere and calcination temperature on the derived ZnO/C composites. Therefore, this work provides a novel insight to understand the role of ZnO and carbon species in MOF-5 derived nanocomposites for the adsorption and photodegradation of MB. To achieve this purpose, we used as-synthesized MOF-5 as precursor to obtain ZnO/C at 800 and 1000 °C under a variety of gaseous atmospheres. In order to control the C to ZnO ratios in the nanocomposites with different functional groups, water was introduced as a weak oxidizing agent to conduct a mild oxidation process at high temperatures without compromising the sample morphologies. The controlled introduction of an oxygen source enables the targeted oxidation of carbon and cationic Zn^{2+}, resulting in the formation of homogeneously dispersed porous ZnO/C with modified energy band gap. Along with the retained morphology, the formed defects and oxygen-containing functionalities, the obtained ZnO/C lead to excellent methylene blue (MB) adsorption and photodegradation performances under visible light irradiation.

Therefore, this work contributes to comprehensive understanding of the behaviors of adsorption and photodegradation of organic dyes on MOF-5 derived ZnO/C nanocomposites under visible light irradiation. Based on our study, it can be established that pure carbon sample **C-Ar$_{1000}$** shows only adsorption without any dye degradation under visible light. MOF derived pure ZnO nanoparticles samples exhibit no adsorption but photodegradation of MB under visible light. However, the samples prepared under argon saturated water vapors show both adsorption and photodegradation of MB. It is observed that photodegradation of MB is more dominant in **ZnO/C-Ar+W(S)$_{800}$** due to the high content of ZnO whereas adsorption of MB is dominated in **ZnO/C-Ar+W(S)$_{1000}$** due to the high level of porous carbon.

2. EXPERIMENTAL SECTION

2.1. Synthesis of MOF-5. All chemicals were purchased from Sigma-Aldrich and used without further purification. To synthesize MOF-5, we followed slightly modified scheme which was first reported by Yaghi *et.al.*[12] Typically, 3.569 g of $Zn(NO_3)_2 \cdot 6H_2O$ (12 mmol) was dissolved in 40 mL of dimethylformamide (DMF) and stirred at room temperature for 15 minutes; meanwhile, in a separate bottle, 0.665 g of terephthalic acid (H_2BDC) (4 mmol) and 3 mL of triethylamine (TEA) were dissolved in 60 mL DMF and stirred for 15 min at room

temperature. Then the solution of $Zn(NO_3)_2 \cdot 6H_2O$ was poured slowly into the H_2BDC solution under constant stirring. The mixed solution was transferred into a 250 mL screw jar, which was closed tightly and put into an oil bath at 110 °C for 20 hours under constant stirring. After cooling down, the white product was washed with DMF and chloroform twice and collected by centrifugation. The obtained products were dried in a vacuum oven at 80 °C overnight.

2.2. MOF-5 Derived ZnO/C Nanocomposites. The as-prepared MOF-5 was used as precursor to prepare porous ZnO/C nanocomposites. For this purpose, 0.20 g of MOF-5 was loaded in an alumina boat and placed in the center of a flow-through quartz tube sitting in a tube furnace. The furnace was set at a ramp rate of 10 °C/min to the target temperature with a dwell time of 1 hour for each sample. The first series of four composites were obtained at 800 °C in air, argon, argon saturated with water vapors introduced only during 1 hour dwell time (for short time duration; S) and argon with saturated water vapors introduced throughout the entire heat treatment (for longer time duration; L) and the resulting samples were named as $ZnO\text{-}Air_{800}$, $ZnO/C\text{-}Ar_{800}$, $ZnO/C\text{-}Ar+W(S)_{800}$ and $ZnO/C\text{-}Ar+W(L)_{800}$ respectively. Following the same gaseous atmospheres and protocols, the second series of four composites were prepared at 1000 °C and the resulting samples were labelled as $ZnO\text{-}Air_{1000}$, $C\text{-}Ar_{1000}$, $ZnO/C\text{-}Ar+W(S)_{1000}$ and $ZnO/C\text{-}Ar+W(L)_{1000}$ respectively.

2.3. Material Characterization. The as-synthesized composites were used for characterizations and photocatalytic applications without further treatment.[27-29] Powder X-ray diffraction (PXRD) patterns were recorded by employing Bruker D8 instrument with Cu Kα radiation (1.54 Å) (40 kV, 40 mA). The powder samples were prepared by gently pressing the powder onto a glass slide. For MOF-5, XRD pattern were recorded in the *2θ* range from 5° to 40° whereas the PXRD patterns of the MOF derived composites were measured in the *2θ* range from 10° to 80°. The morphologies, elemental compositions and elemental mapping of the as-prepared composites were characterized by scanning electron microscopy (SEM) (Hitachi S3200N) and transmission electron microscopy (TEM) (JEM 2100 LeB6 200 KV) equipped with energy dispersive X-ray spectroscopy (EDS). For SEM, powder samples were spread on a carbon tape and sputtered with a gold layer of 5 nm thickness. For TEM images and elemental mapping, the samples were first dispersed in absolute ethanol under moderate sonication and then pipetted onto a holey carbon Cu grid. Thermogravimetric analysis and mass spectroscopy

(TGA-MS) were carried out on a TA SDT Q600 instrument coupled with Hiden QGA gas analysis mass spectrometer to detect the gas compositions from the exhaust emission. For TGA-MS, 10 mg of each sample was put into an alumina crucible and heated from 20 to 810 °C with a heating rate of 10 °C/min under an air flow of 100 mL/min. The Raman spectra were recorded (WITec ALPHA300 R) by using 532 nm laser excitation under 6 mW in a range from 20 to 2000 cm^{-1}. Fourier-transform infrared (FTIR) spectra of the samples were recorded with an Alpha Bruker system. For each sample, a small amount of sample was mixed with KBr powder and pressed in the form of a pallet for the FTIR analysis. The X-ray photoelectron spectroscopy (XPS) was performed using a Kratos AXIS ULTRA spectrometer with a monochromated Al KR X-ray source (1486.6 eV) operated at 10 mA emission current and 15 kV anode potential. The analysis chamber pressure was better than 1.3×10^{-12} bar. The take-off angle for the photoelectron analyzer was 90° and the acceptance angle was 30°. The energy band gaps of the ZnO and ZnO/C nanocomposites were calculated from diffuse reflectance spectra acquired by employing a spectrophotometer (PerkinElmer lambda 1050 with 150 mm integrated InGaAs sphere). The specific surface areas (SSA) and the pore size distributions (PSD) of the composites were measured on a Micromeritics 3Flex instrument. Prior to the measurements the samples were degassed at 200 °C for 3 hours. The N_2 gas used had a purity of 99.999 %. The BET surface area was calculated using the Rouquerol correction for microporous solids. The pore size distribution was determined using nonlocal DFT with the Tarazona model for nanoporous materials with cylindrical pores.

2.4. Evaluation of Adsorption/Photodegradation Activity. Adsorption of methylene blue (MB) from water solution on the as-synthesized ZnO/C nanocomposites was evaluated in a dark box. Typically, 10 mg of as-prepared sample was added into 50 mL of 20 ppm aqueous MB solution. The suspension was immediately transferred to a dark box under constant stirring. After different intervals of time, 1 mL aliquots were taken and the concentration of MB in the solution was determined by UV-vis absorption spectroscopy. Using a similar procedure, the synergistic adsorption and photodegradation of MB by ZnO/C composites were measured under visible light irradiation. The visible light source (cutoff filter, $\lambda>420$ nm) was provided by 10 lamps of 20 W with a light intensity of 160 mW/cm^2 (PerfectLight, 320 nm $\leq \lambda \leq$ 780 nm). The adsorption/photodegradation of MB (%) was calculated by using the following expression:

$$D (\%) = \frac{C_o - C}{C_o} \times 100\% \qquad (1)$$

Where D is the percentage of degradation, C_o is the initial concentration and C is the final concentration.[29] To measure the recyclability and stability of the material, the best performing sample **ZnO/C-Ar+W(S)$_{1000}$** was separated from solution by filtration using a filter paper. Before reusing for the next run, the filtered sample was washed with deionized water several times and dried in oven at 110 °C for 2 hours. The sample was consecutively used for 5 cycles.

3. RESULTS AND DISCUSSION

3.1. Characterizations of the Composites.
The crystal structures and phase transformations of the nanocrystalline MOF-5 and obtained derivatives were examined by Powder X-ray diffraction (PXRD) as shown in Figure 1. The PXRD pattern of as-synthesized MOF-5 (Figure S1) exhibits reflections at $2\theta = 6.8°$ and $9.7°$, which is in agreement with the theoretically predicted PXRD pattern of MOF-5 synthesized by the direct mixing method.[28-31]

Heat processing of MOF-5 at high temperature in air flow results in white colored pure ZnO nanoparticles. The samples **ZnO-Air$_{800}$** and **ZnO-Air$_{1000}$** show diffraction peaks at 2θ of $31.7°$, $34.4°$, $36.2°$, $47.5°$, $56.5°$, $62.8°$, $66.3°$, $67.9°$, $72.5°$ and $76.9°$ which confirm the polycrystalline wurtzite structure of ZnO.[27, 32] **ZnO-Air$_{1000}$** shows much stronger diffraction peaks than **ZnO-Air$_{800}$**, indicating higher crystallinity of the ZnO nanoparticles. However, black products were generated upon heat treatment in argon and water vapors, signifying the carbonization of precursor. Heat processing of MOF-5 in Ar atmosphere, a significant amount of ZnO appears in the sample **ZnO/C-Ar$_{800}$** whereas no ZnO is observed in the PXRD patterns of sample **C-Ar$_{1000}$**. This may be due to the fact that while the heat process temperature is above the boiling point of Zn (907 °C), the formed Zn is likely to evaporate. Consequently, no diffraction peaks belonging to Zn or ZnO species can be observed in the powder diffraction pattern of **C-Ar$_{1000}$**. A broad reflection centered at around $2\theta = 23°$ is due to the (002) lattice plane reflection of graphitic carbon species. The broadening of this diffraction peak indicates the low degree of graphitization, confirming the amorphous nature of the formed carbon.[30- 33] It can be observed that the diffraction peak intensities of ZnO/C are weaker as compared to pure ZnO samples. It indicates that the samples obtained in Ar and H_2O atmosphere at 800 °C possess relatively lower

crystallinity and smaller particle sizes. The closer observation (Inset to Figure 1a) shows that in sample **ZnO/C-Ar+W(S)$_{800}$** the strongest diffraction peak (101) of ZnO shifts slightly from 36.24º to 36.18 º 2θ. Such diffraction shifting compared to pure ZnO is assigned to doping induced unit cell deformation. It is further confirmed by DRS, FTIR and Raman spectroscopy that change in ZnO lattice parameters and structural deformation can be attributed to the induced defects and narrow energy band gap.

The nanocomposite **ZnO/C-Ar+W(L)$_{1000}$** shows broad reflections representative for amorphous carbon as well as the very low intensity peaks of ZnO. However, the **ZnO/C-Ar+W(S)$_{1000}$** showed only the broader diffraction peak of amorphous carbon. The intensities of the ZnO reflections in all samples obtained in Ar and H$_2$O atmosphere at 1000 °C are negligible compared with the samples prepared at 800 °C, most likely due to the relative very low content of ZnO in those samples, as shown in the TGA-MS measurements below. Compared with sample **C-Ar$_{1000}$**, the diffraction peaks of amorphous carbon for the water vapors processed samples remained unaffected by water vapors atmosphere that clearly indicated the preservation of a carbon structures under these conditions, which was also confirmed by Raman spectroscopy and XPS analysis. Due to the high intensity of the ZnO reflections for all the composites derived at 800 °C, the diffraction peak for amorphous carbon is suppressed. From the PXRD results, it is evident that the heat process temperature as well as the heat treatment atmosphere during the carbonization process has a significant impact on the nature of the resulting metal oxide/carbon nanocomposites.
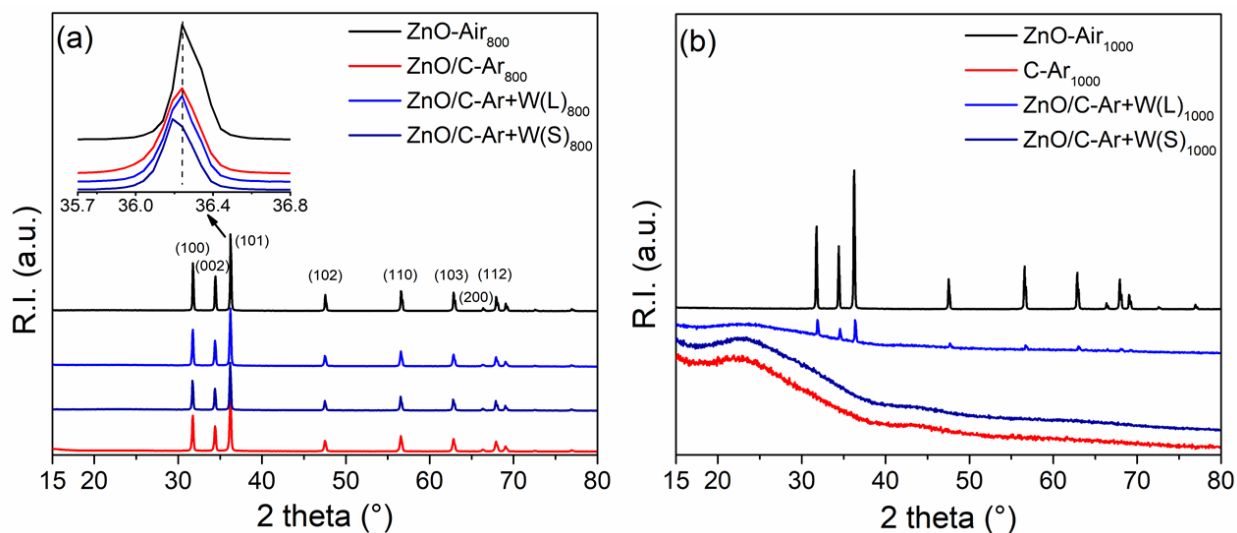
Figure 1. PXRD patterns of nanocomposites obtained in different carbonization atmospheres at 800 °C (a) and 1000 °C (b). **ZnO-Air, ZnO/C-Ar+W(L), ZnO/C-Ar+W(S)** and **ZnO/C-Ar** are represented in black, light blue, dark blue and red, respectively. Numbers in brackets mark the miller indices of the lattice plane reflections of the wurtzite modification of ZnO. Inset to Figure 1(a) is the amplified PXRD pattern of peak (101).

TGA-MS was carried out under air flow to evaluate the thermal stabilities of nanocomposites as well as to determine the amount of carbon and other species presented in the as-synthesized nanocomposites. The TGA profile of the as-synthesized MOF-5 in Figure 2a shows 20 % weight loss in the first step at around 200 °C due to the evaporation of the solvent DMF and adsorbed moisture and further 40 % weight loss in the second step at around 500 °C due to the decomposition of the organic linker.
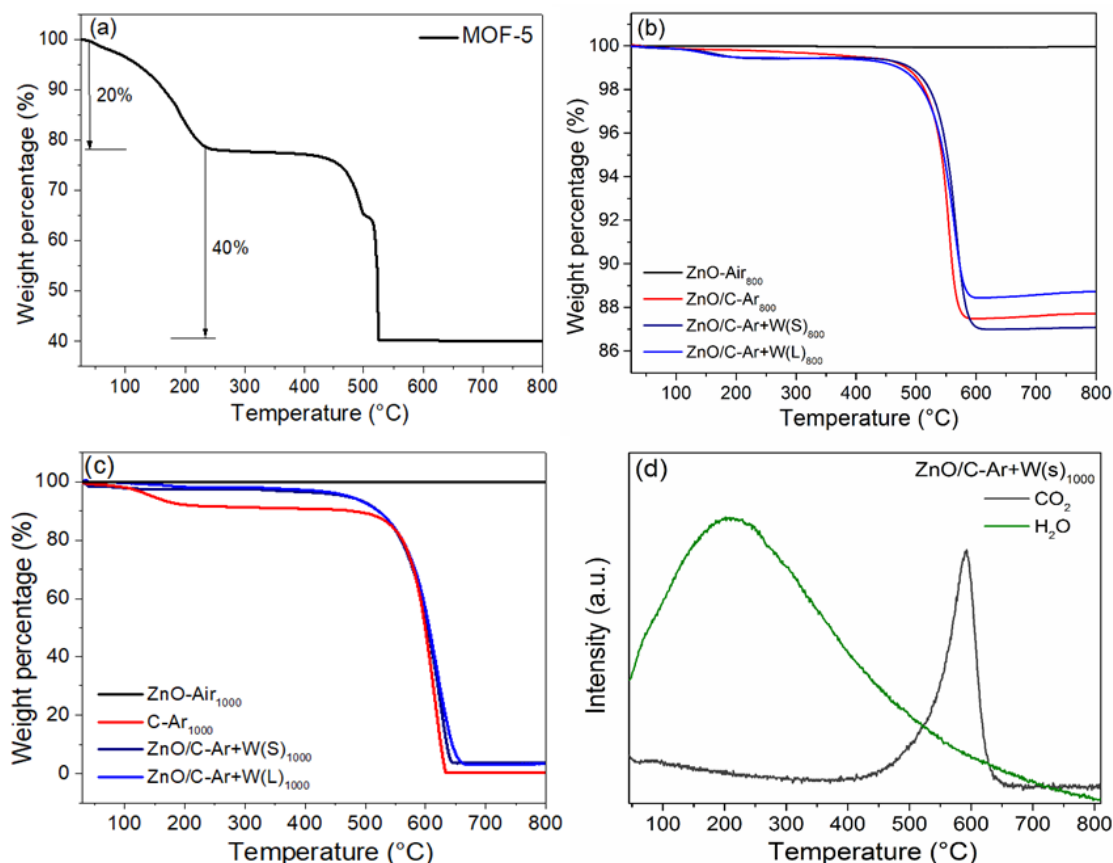

Figure 2. TGA profiles of MOF-5 (a) and derived composites (**ZnO-Air** (black)**, ZnO/C-Ar+W(L)** (blue)**, ZnO/C-Ar+W(S)** (dark blue) and **ZnO/C-Ar** (red)) obtained under different

gaseous atmospheres at 800 °C (b), 1000 °C (c) and temperature dependent mass spectra (d) surveying H_2O and CO_2 release during heat treatment of **ZnO/C-Ar+W(s)$_{1000}$**.

Figure 2b and c represent the TGA profiles of composites obtained at 800 and 1000 °C respectively. **ZnO-Air$_{800}$** and **ZnO-Air$_{1000}$** are pure wurtzite polycrystalline ZnO derived from MOF-5 and show no weight loss in the applied temperature range, confirming the absence of carbon in these samples. However, sample **C-Ar$_{1000}$** lost around 10% mass at 100 °C, implying the removal of adsorbed moisture and further weight loss of the remaining 90% mass at around 650 °C, indicating that only carbon is presented in this sample with no residual species. This is clearly due to the complete evaporation of Zn species during the carbonization process that results in the generation of pure porous carbon. The composites **ZnO/C-Ar$_{800}$**, **ZnO/C-Ar+W(S)$_{800}$** and **ZnO/C-Ar+W(L)$_{800}$** exhibit 11 % to 13 % weight loss at around 550 °C due to the burn-off of carbon, which suggests that these composites contain up to 87-89% of ZnO. However, the composites **ZnO/C-Ar+W(S)$_{1000}$** and **ZnO/C-Ar+W(L)$_{1000}$** contain around 96% of carbon. The mass spectra in Figure 2(d) further confirms that the weight loss upon heating in air is due to the release of adsorbed moisture (H_2O) at lower temperature and burn-off of carbon to form CO_2 at higher temperature up to 600 °C. Due to the presence of oxygen species in the carbonization atmosphere, a very samll amount of ZnO was retained in the composites regardless of the carbonization temperatures. The obtained TGA-MS results show good consistency with the PXRD patterns. It is observed that the short time water exposure (**S**) and longer time moisture exposure during the entire carbonization process (**L**) has less influence on the ZnO content in the composites. However, the longer exposure to moisture has considerable impact on the specific surface areas and functionalization of composites as confirmed by BET, FTIR and Raman spectroscopies. The composites derived at 1000 °C demonstrated increased thermal stability in comparison to the composites obtained at 800 °C.

The morphologies of the MOF-5 precursor and its derived composites were analyzed by scanning electron microscopy (SEM) and transmission electron microscopy (TEM). Well-defined cubic crystals of MOF-5, approximately 1 µm in size are clearly observed in the SEM micrographs shown in Figure 3a and b. Upon heating to elevated temperatures and carbonization, the material retained its cubic morphology which is in agreement with previous reports.[34] In spite of different carbonization atmospheres, no morphological differences are observed in samples

synthesized at 800 °C. However, at treatment temperatures of 1000 °C, most of the ZnO reduced to Zn and evaporated, leaving behind smaller porous carbon particles with high surface areas confirmed by gas sorption analysis. More hollow and partially broken cubic porous carbon structures can be seen in Figure 3d. Srinivas *et al.* argued that this process can be called a self-activation of carbon, which is predominantly influenced by the framework structures, metal centers and initial porosities of the precursor MOFs.[34] The SEM images of samples **ZnO/C-Ar₈₀₀** and **ZnO/C-Ar+W(L)₈₀₀** are shown in Figure S5a and b confirming that the morphologies of the composites are retained in all atmospheric conditions. After using of composite **ZnO/C-Ar+W(S)₈₀₀** for dye photodegradation, SEM images were taken (Figure S5c and d). No visible morphological changes are observed.
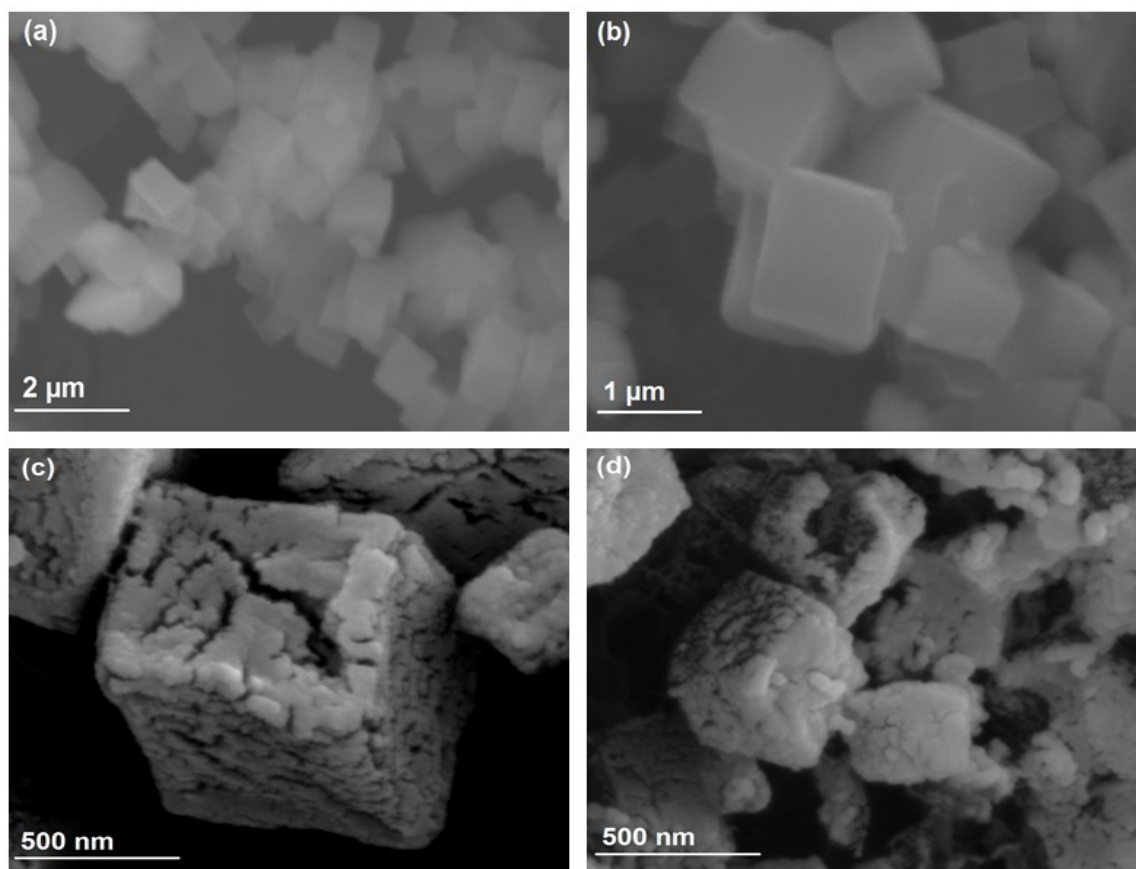

Figure 3. Representative SEM micrographs of MOF-5 (a, b), **ZnO/C-Ar+W(S)₈₀₀** (c) and **ZnO/C-Ar+W(S)₁₀₀₀** (d).

Representative TEM images of selected composites **ZnO/C-Ar+W(S)800** and **ZnO/C-Ar+W(S)1000** are presented in Figure 4. The low magnification images (Figure 4a and d confirm the topology of the derived composites. In the High-resolution TEM (HR-TEM) images (Figure 4c and f, the nanosized ZnO particles embedded in the transparent layers of porous carbon are evident. The estimated sizes of these ZnO nanoparticles lie in the range of 5-10 nm. Figure S6 shows the HRTEM image of selected sample **ZnO/C-Ar+W(s)800** where the fringes of ZnO crystal lattice can be clearly seen. Figure 5.The homogeneous dispersion of ZnO nanoparticles (Figure 5) in porous carbon matrices is further confirmed by elemental mapping. The composite **ZnO/C-Ar+W(S)800** exhibits homogeneous distribution of zinc, oxygen and carbon throughout the selected sample area. The elemental mapping of the composite **ZnO/C-Ar+W(S)1000** shows the uniform dispersion of C with negligible amount of Zn and O, due to the high C content of 96% in this sample. As confirmed by XRD and TGA (Figure 1a and Figure 2b), homogeneously distributed ZnO nanoparticles in a porous carbon framework can be achieved upon high-temperature carbonization of highly crystalline MOF-5 in water saturated argon atmosphere.[27] The nanoparticles with such small sizes usually show broader XRD peaks. However, in these samples, the peaks are of relatively high intensity. It can be understood in this way that we use MOF-5 as precursor, which contains Zn, C, O and during the carbonization process, the benzene rings will carbonize to form amorphous porous carbon, while the Zn will migrate to combine with O to form ZnO. Although many of the formed ZnO particles with small size (such as 5-10 nm) are surrounded by the formed amorphous porous carbon, under high temperature pyrolysis conditions, some small ZnO particles are inevitably migrate together to form bigger ZnO particles due to the high surface energy of the small ZnO particles. Therefore in the XRD, the strong diffraction peaks from the bigger ZnO makes it difficult to see the contribution from small particles. In Figure 4b and e, the dark spots of isolated bigger ZnO nanoparticles can be seen.
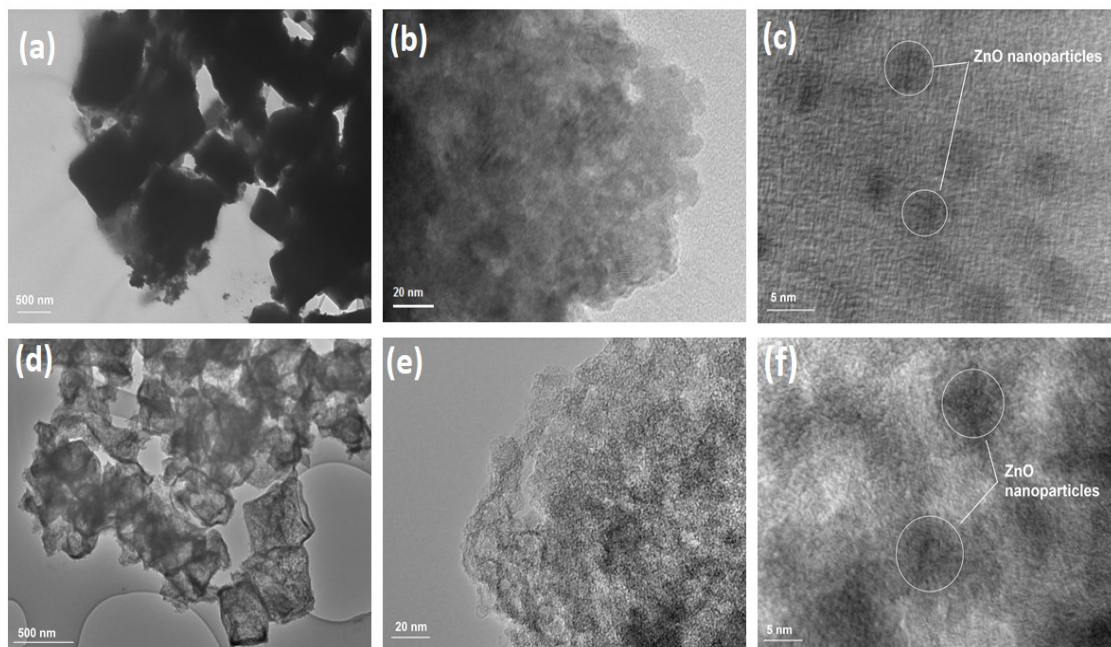
Figure 4. TEM and HRTEM images of **ZnO/C-Ar+W(S)$_{800}$** (a, b, c) and **ZnO/C-Ar+W(S)$_{1000}$** (d, e, f) at different magnifications.
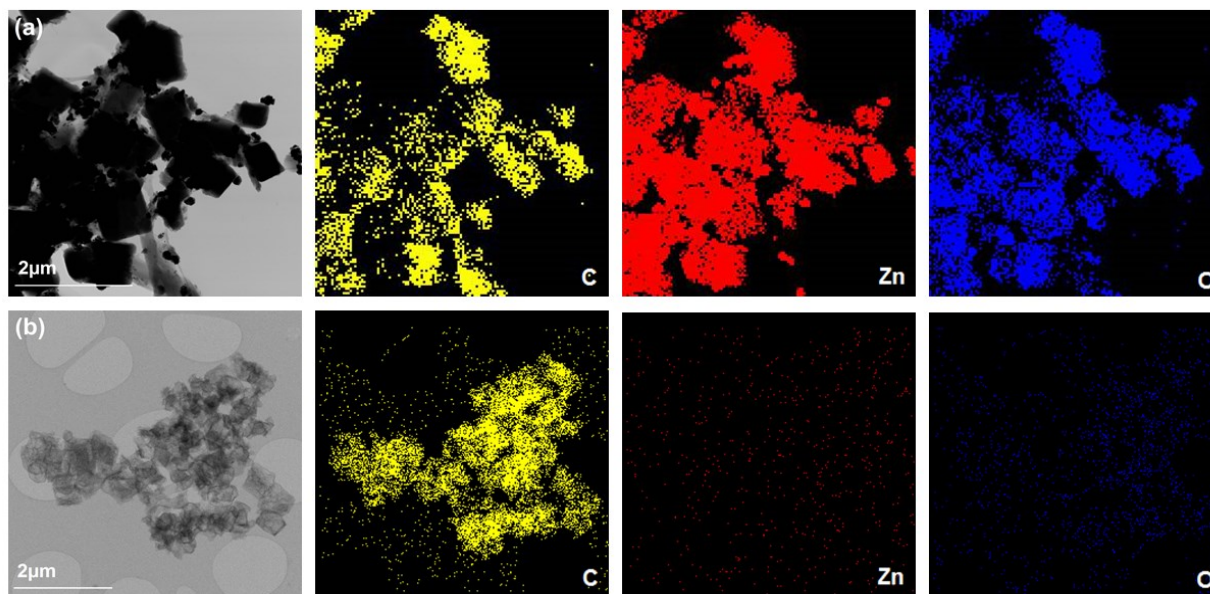

Figure 5. TEM micrographs and elemental maps of **ZnO/C-Ar+W(S)$_{800}$** (a) and **ZnO/C-Ar+W(S)$_{1000}$** (b). The elemental maps were obtained by EDS. The colored images show the

distribution of elements throughout the composite. C, Zn, and O are represented in yellow, red and blue, respectively.

To study the nature of the carbon presented in these nanocomposites and lattice vibrational modes of ZnO, Raman spectra of all materials were recorded (Figure 6a and Figure S2a). The composites **ZnO-Air$_{800}$** and **ZnO-Air$_{1000}$** show strong signals for highly crystalline MOF-5 derived pure ZnO nanoparticles with main peaks occurring at 438 and 454 cm^{-1} due to E$_2$(high) mode respectively. The other peaks at around 332 and 347 cm^{-1} in these samples correspond to A$_1$(TO) mode (second order Raman processes) of ZnO. For bulk ZnO, these signals appear at 475 cm^{-1}.[35-38] The E$_2$ phonon frequency usually occurs at around 436 cm^{-1} for ZnO quantum dots (QDs) with sizes less than 10 nm.[37] The observed ZnO peaks indirectly confirms the particle sizes observed by HRTEM. It should be noted that in MOF-5 derived ZnO/C at 800 °C, these E$_2$(high) and A$_1$(TO) modes red shifted to 427 and 321 cm^{-1} compared to pure ZnO (Inset to Figure 6a). The observed red shift (to lower wavenumbers) in mode positions can be ascribed to the strain on the ZnO due to the presence of carbon atoms in the crystal lattice. Red shift in Raman spectra also takes place when the incident photons lose energy upon interaction with the vibrational modes of the material (phonons). This energy is absorbed by the material leading to the peak shift toward lower frequencies. It suggests that the doped carbon atoms alter the bond lengths and the lattice parameters of ZnO, generating new crystalline lattice defects and eventually narrowing the energy band gap. This red shift in frequencies is also observed in FTIR spectra of ZnO/C composites shown in Figure S3.

Two characteristic signals of amorphous carbon are observed at around 1350 and 1590 cm^{-1} for all samples obtained under argon and water vapor atmosphere at 800 and 1000 °C. In the samples **ZnO/C-Ar$_{800}$**, **ZnO/C-Ar+W(S)$_{800}$** and **ZnO/C-Ar+W(L)$_{800}$**, the G band at around 1588 cm^{-1} is generated by the formation of nanocrystalline carbon, and represents the bond stretching of all sp^2 atoms in both, all carbon hexagonal rings and chains. The D band at around 1348 cm^{-1} is due to the breathing modes of sp^2 hybridized carbon atoms in hexagonal rings, which signifies the formation of amorphous carbon. This mode is forbidden in perfect graphite crystals and it can only be seen in the presence of disorder in structure. The intensity of the D band and particularly the I$_D$/I$_G$ ratio is a measure for the content of defects and disorder in the crystalline carbon structures.[39-41]

15

As shown in Figure 6a and Figure S2a, the comparison of the I_D/I_G ratios of the composites **ZnO/C-Ar$_{800}$** (0.82), **ZnO/C-Ar+W(S)$_{800}$** (0.82) and **ZnO/C-Ar+W(L)$_{800}$** (0.86) with **C-Ar$_{1000}$** (0.99), **ZnO/C-Ar+W(S)$_{1000}$** (0.89) and **ZnO/C-Ar+W(L)$_{1000}$** (0.84) reveal that increasing the annealing temperature increases the I_D/I_G ratio which indicates that the high temperature and longer exposure to the water vapors during the carbonization process generate more defects in the carbon matrix, eventually enhancing the amorphous nature of the composites.[41-43]
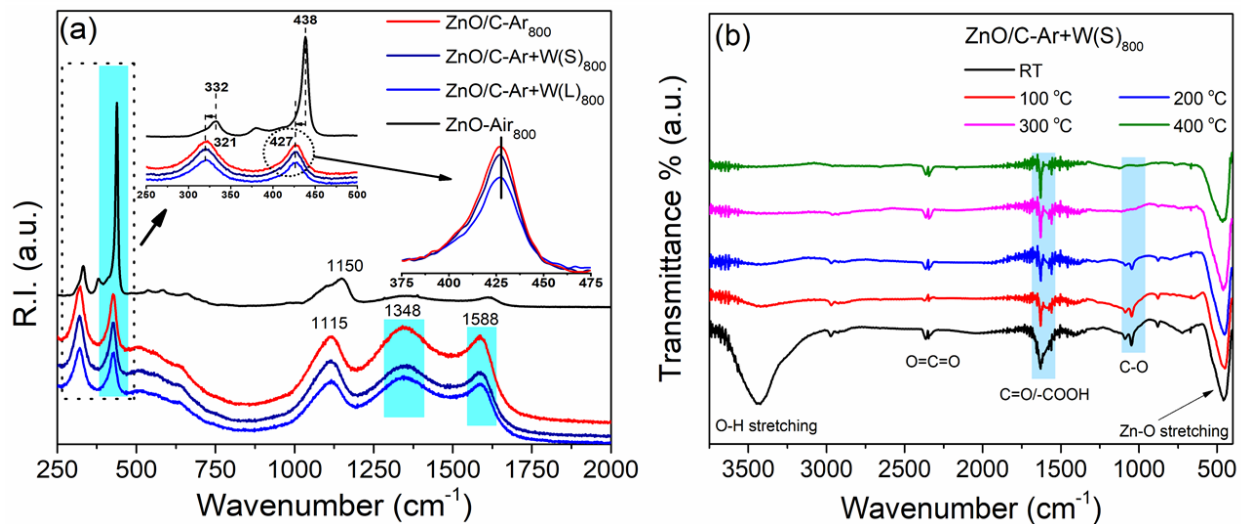

Figure 6. Raman Spectra of **ZnO-Air** (black), **ZnO/C-Ar** (red), **ZnO/C-Ar+W(S)** (dark blue) and **ZnO/C-Ar+W(L)** (light blue) prepared at 800 °C (a). FTIR spectra of **ZnO/C-Ar+W(S)** derived at 800 °C (b) after treatment of the materials at RT (black), 100 °C (red), 200 °C (blue), 300 °C (pink) and 400 °C (green), respectively.

FTIR was employed to investigate the presence of functional groups on the surface of the nanocomposites. The FTIR spectra of selected samples **ZnO/C-Ar+W(s)$_{800}$** and **ZnO/C-Ar+W(s)$_{1000}$** were recorded at room temperature. As shown in Figure 6b, **ZnO/C-Ar+W(s)$_{800}$** exhibits a strong band at 460 cm^{-1} which is attributed to the Zn-O stretching from the crystalline wurtzite ZnO. This signal in **ZnO/C-Ar+W(s)$_{1000}$** is negligible (shown in Figure S2b), due to the much lower ZnO content in this sample, as demonstrated in XRD, XPS and TGA analysis. A strong signal is observed at around 1630 cm^{-1} in both samples, which is assigned to the C-OH and C=O bond stretching of –OH and –COOH groups. A comparatively weak band at 2360 cm^{-1} in these samples is ascribed to O=C=O bond stretching. A broader signal at 3445 cm^{-1} indicative for O-H/Zn-OH bond stretching of adsorbed H_2O is observed in both samples.[1]

To confirm the presence of carboxylate (–COOH) groups on the surface of the nanocomposites, the sample was heated in a furnace at 100, 200, 300 and 400 °C for 1 hour and then the FTIR spectra were recorded subsequently. It was found that the signal at 1630 cm^{-1} became more prominent in both samples during heating, which confirms the presence of -COOH functional groups. This effect is accompanied by the decrease of the broad O-H stretching vibrations at 3445 cm^{-1} and C-H stretching at 2972 cm^{-1}, indicating the gradual evaporation of the adsorbed H$_2$O. The FTIR spectra of **ZnO-Ar$_{800}$**, **ZnO-Ar+W(S)$_{800}$**, **ZnO/C-Ar+W(L)$_{800}$** and **ZnO-Air$_{800}$** are presented in Figure S3. The relatively stronger peak at 1630 cm^{-1} in **ZnO-Ar+W(S)$_{800}$** (Inset to Figure S3) confirms that there is higher concentration of –COOH functional group present in this sample compared to other prepared composites.

To further analyze the elemental compositions of the derived composites, the XPS spectra of selected samples are presented. As shown in Figure 7a, the wide elemental spectra confirm the presence of Zn, O and C in all the composites obtained at 800 °C. In the Zn 2p spectrum, the Zn 2p$_{3/2}$ and 2p$_{1/2}$ doublet (Figure 7b) appear at binding energies of 1021.05 and 1044.15 eV, respectively. The binding energy distance between 2p$_{3/2}$ and 2p$_{1/2}$ (23.1 eV) energy levels implies the presence of Zn^{2+} ions. The Zn peak is stronger in pure ZnO sample whereas the intensity reduces in composites **ZnO/C-Ar$_{800}$** and **ZnO/C-Ar+W(S)$_{800}$** with a blue shift in binding energy from 1021.05 to 1021.15 eV, maybe due to the carbon doping into the ZnO lattice. Deconvoluting the Zn 2p$_{3/2}$ peak of **ZnO/C-Ar+W(S)$_{800}$**, two components can be seen at 1020.9 and 1021.2 eV which can be ascribed to Zn-O-C due to the doped carbon and Zn-O bond respectively.[44] As shown in Figure 7c, the main peak of O$_{1s}$ in sample **ZnO-Air$_{800}$** is observed at 530.13 eV with a small shoulder at 531.59 eV. These peaks are allocated to the Zn-O bond and surface adsorbed oxygen species, respectively.[7] For the sample **ZnO/C-Ar$_{800}$**, O1s peak at 530.35 and 531.74 eV can be ascribed to Zn-O bond, metal carbonate species such as C-O / C=O bonds or surface adsorbed oxygen species respectively. However, for the sample **ZnO/C-Ar+W(S)$_{800}$**, O$_{1s}$ peaks can be deconvoluted into three separate peaks centered at 530.27, 530.99 and 532.19 eV. These peaks can be assigned to the Zn-O bond, carbonate species (C-O)/C=O) and carboxylic functional group –COOH introduced through water steam atmosphere during carbonization of MOF-5 respectively.[45, 46]
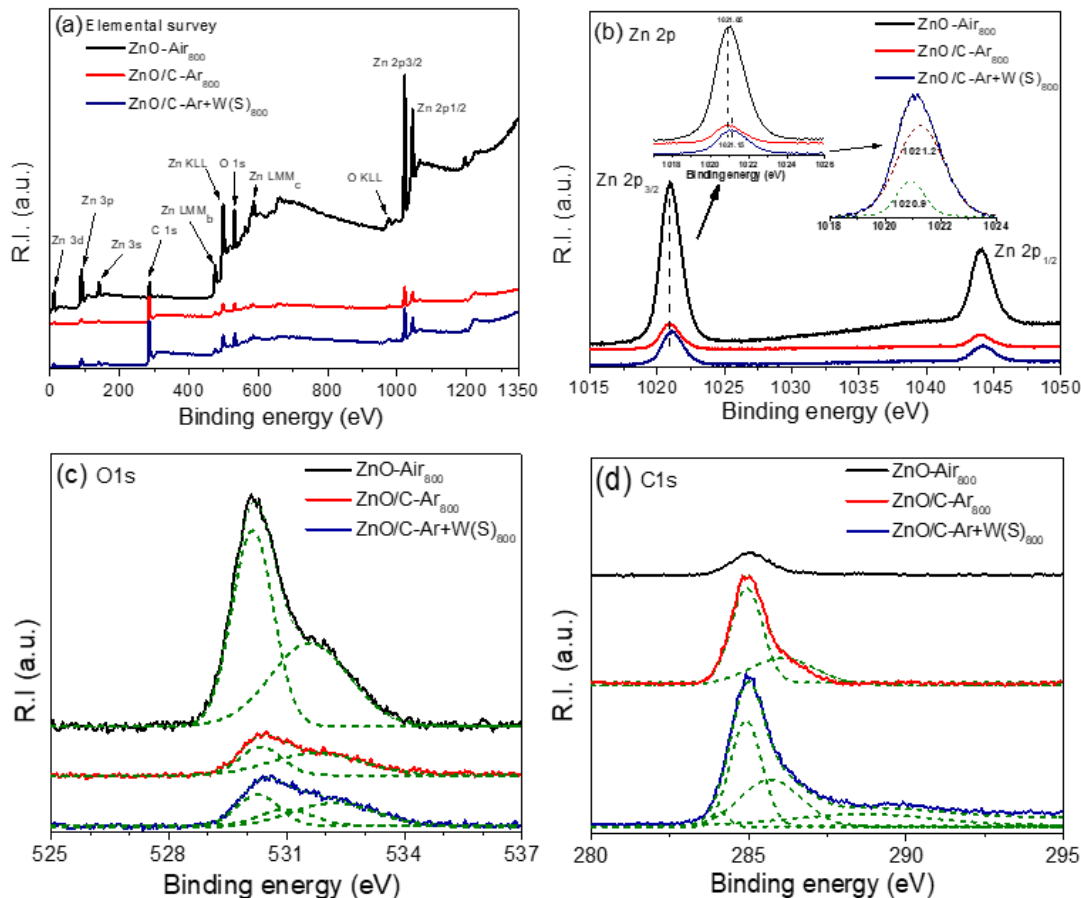
Figure 7. XPS spectra of elemental survey (a) Zn 2p (b) O 1s (c) C 1s (d) for **ZnO-Air$_{800}$** (black) and **ZnO/C-Ar$_{800}$** (red) and **ZnO/C-Ar+W(S)$_{800}$**(Dark blue).

The C$_{1s}$ spectra (Figure 7d) of samples **ZnO/C-Ar$_{800}$** and **ZnO/C-Ar+W(S)$_{800}$** show main peaks at 284.9 eV. It is in good agreement with the reported C-C bond of sp^2 hybridized graphitic carbon confirmed by Raman results.[47] The other deconvoluted peaks of C1s in **ZnO/C-Ar$_{800}$** and **ZnO/C-Ar+W(S)$_{800}$** appear at around 286 eV can be ascribed to carbonate species with different amount of C=O/C-O bonds. A small C1s peak appeared at 284.1 eV in **ZnO/C-Ar+W(S)$_{800}$** can be assigned to Zn-C bond.[48] The low intensity of this peak shows that there is only small amount of carbon is doped into the ZnO lattice. A broader peak at 288.9 arises due to the presence of –COOH functional group as confirmed by O1s XPS peak as well as FTIR spectra (Figure 6b).[7] The higher intensity of O$_{1s}$ and C1s in **ZnO/C-Ar+W(S)$_{800}$** as compared to **ZnO/C-Ar$_{800}$** provides the evidence of successful incorporation of other oxygen species (-

18

COOH functional groups) into the composites. A low intensity peak for carbon in the pure **ZnO-Air$_{800}$** is also observed at 285.1 eV, which may due to the background and sample holder.

The specific surface areas and pore size distributions of the nanocomposites were determined by N_2 physisorption at 77 K and the isotherms are shown in Figure 8 and Figure S4 respectively. Due to the capillary filling of the micropores, all samples showed type I isotherms. As shown in Figure 8a and b, the adsorption is reversible which verifies the predominant microporous nature of these composites. The composites **ZnO/C-Ar$_{800}$**, **ZnO/C-Ar+W(S)$_{800}$** and **ZnO/C-Ar+W(L)$_{800}$** exhibits BET surface areas of 369, 350 and 210 m^2/g respectively. The BET surface areas of the composites **C-Ar$_{1000}$**, **ZnO/C-Ar+W(S)$_{1000}$** and **ZnO/C-Ar+W(L)$_{1000}$** derived at 1000 °C are measured to be 2839, 2390 and 2600 m^2/g respectively, much higher than those samples derived from 800 °C. These exceptional BET surface areas of composites **C-Ar$_{1000}$**, **ZnO/C-Ar+W(S)$_{1000}$** and **ZnO/C-Ar+W(L)$_{1000}$** originate from the very high surface area of the precursor MOF-5 (3800 m^2/g).[22] Upon carbonization of MOF-5 in Ar above the boiling point of Zn, the Zn metal atoms ionize and evaporate leaving behind highly porous amorphous carbon with partially broken inherited cubic morphology. The retained high porosity and defects in these derived 3D amorphous cubic carbons show high surface areas confirmed by SEM and HRTEM. However, the measured values are still lower than the reported precursor MOF-5.

It is worth noting that the specific surface areas of the composites obtained in Ar atmosphere are higher than the composites obtained in water vapors. It may be due to the water steam causing some ZnO to stay in the pores reducing the overall surface areas. TGA measurements confirmed that there is no ZnO nanoparticles in sample **C-Ar$_{1000}$**, therefore it has the highest specific surface area. In contrast, the nanocomposite **ZnO/C-Ar+W(L)$_{800}$** showed the lowest surface area among these samples.
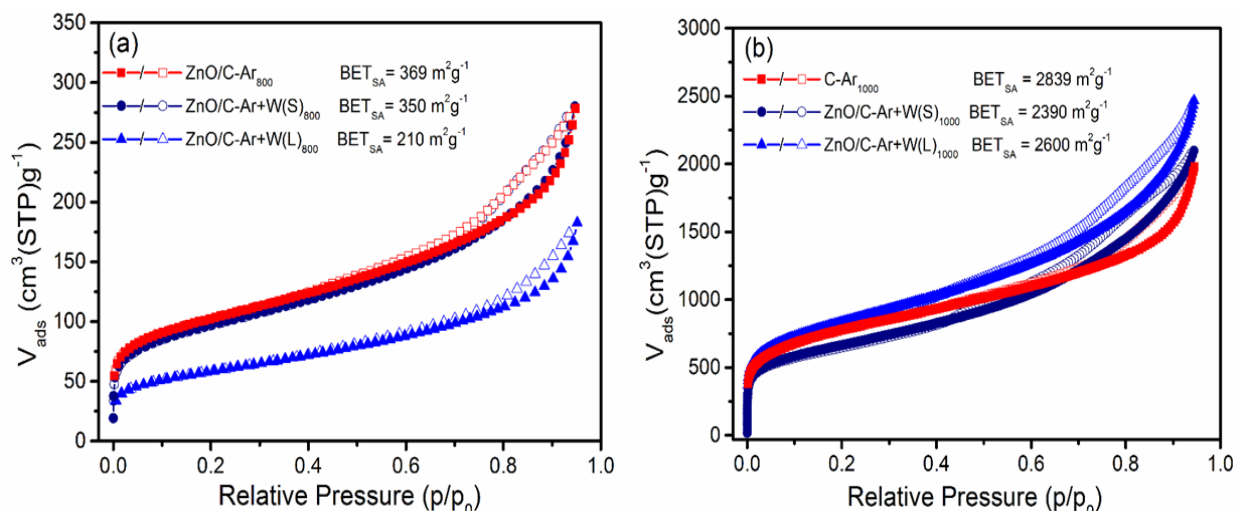
Figure 8. N$_2$ sorption isotherms measured at 77 K for **ZnO/C-Ar** and **C-Ar** (red squares), **ZnO/C-Ar+W(S)** (dark blue circles) and **ZnO/C-Ar+W(L)** (light blue triangles) derived at 800 °C (a) and 1000 °C (b) respectively. Filled and empty symbols represent adsorption and desorption. The lines are a guide to the eye only.

Pore size distributions (PSD) of these nanocomposites were analyzed based on the nitrogen adsorption data using the Non Local Density Functional Theory (NLDFT) model. As shown in Figure S4a and b, the nanocomposites derived at 800 °C and 1000 °C are dominated with PSDs between 10 and 15 Å centering at around 12.3Å. It also confirms that all the derived composites are predominantly microporous regardless of the atmosphere applied.

3.2. Optical Properties and Photocatalytic Dye Degradation Performance. The optical properties of the composites were studied by employing UV-vis diffuse reflectance spectroscopy (DRS). The reflectance spectra of selected nanocomposites are shown in Figure 9a. The reflectance spectra of the composites **ZnO/C-Ar+W(S)$_{800}$** and **ZnO/C-Ar+W(S)$_{1000}$** red shifts to 387 and 395 nm respectively in comparison to pristine **ZnO-Air$_{1000}$** which exhibits the reflectance at 380 nm. The energy band gaps (EBG) of the composites were calculated by using the Tauc plot as shown in Figure 9b. The EBG of MOF-5 derived **ZnO-Air$_{1000}$** was determined as 3.26 eV which is smaller than the EBG of commercially available ZnO nanoparticles (3.37 eV). The EBG of **ZnO/C-Ar+W(S)$_{800}$** and **ZnO/C-Ar+W(S)$_{1000}$** were calculated as 3.0 eV and 3.1 eV respectively. The MOF-5 derived nanocomposites **ZnO/C-Ar+W(S)$_{800}$** and **ZnO/C-Ar+W(S)$_{1000}$** show considerable shifts in EBGs compared to the EBG of the bulk ZnO. The

proposed mechanism of dye photodegradation by ZnO/C composites is shown in Figure 10. Due to the doping of anionic carbon, the valance band of ZnO shifts upwards, resulting the narrow EBG. It should be noted that the EBG strongly correlates with the size and morphology of the nanoparticles. MOF-5 derived ZnO nanoparticles retain the cubic particle shapes of MOF-5 with sizes in the range of 5-10 nm. Therefore, the EBG was predictable to be shifted to longer wavelengths confirmed by Raman, FTIR and XPS results. It can be expected that with the decrease of energy band gaps, these homogeneously distributed ZnO nanoparticles in porous carbon can absorb more visible light which will result in an improved photocatalytic performance.
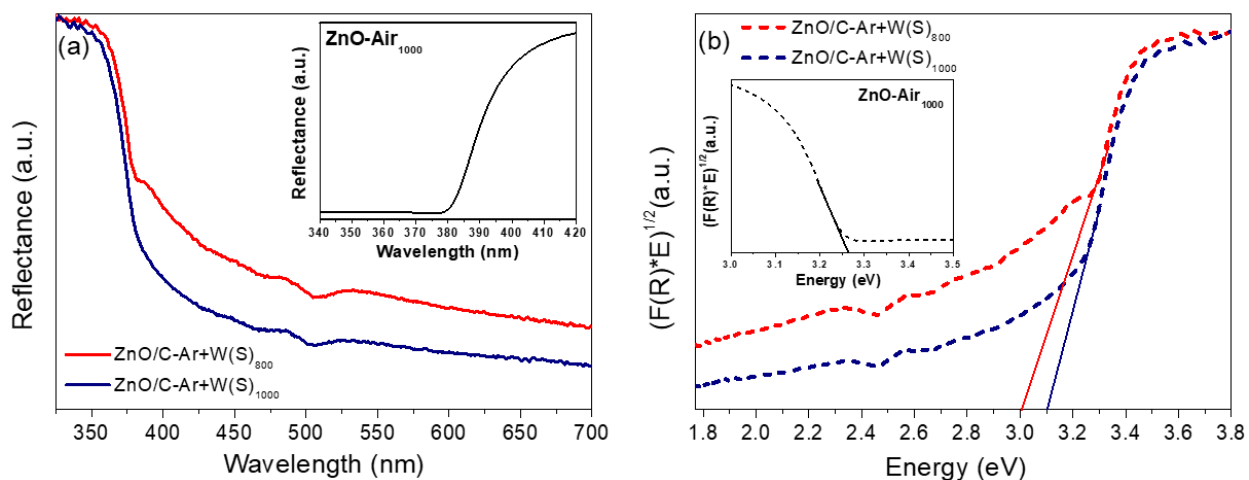

Figure 9: Reflectance spectra of selected samples **ZnO-Air$_{1000}$** (black, insets), **ZnO/C-Ar+W(S)$_{800}$** (red) and **ZnO/C-Ar+W(S)$_{1000}$** (dark blue) (a) and energy band gaps of these composites calculated by the Kubelka-Munk function (Tauc plots) (b).
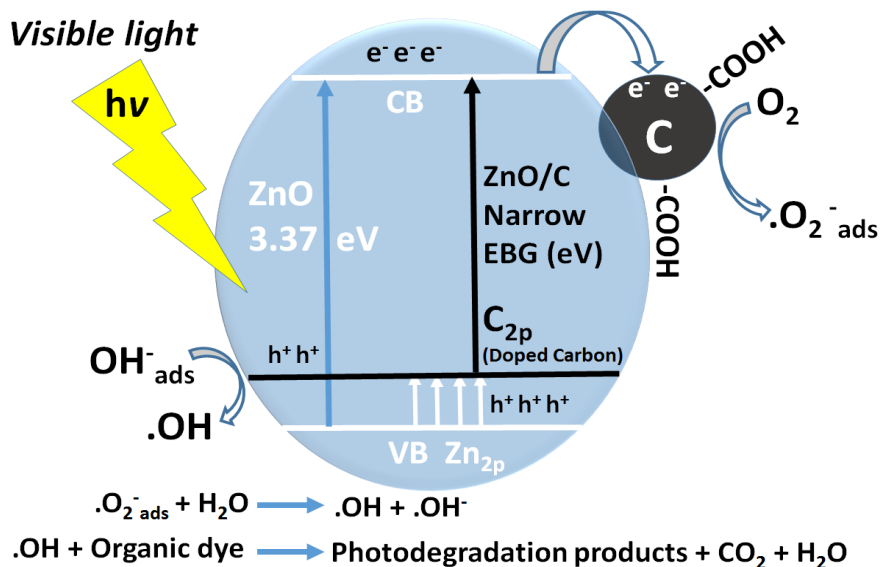
Figure 10: Mechanism of energy band gap shift in MOF derived ZnO/C nanocomposites and the dye photodegradation under visible light irradiation.

To demonstrate the adsorption and photodegradation capacities of the as-synthesized porous ZnO/C nanocomposites, the degradation of methylene blue (MB) was carried out in a dark room and under visible light irradiation respectively. To evaluate the photocatalytic activity of each sample, 10 mg of as-prepared sample was added to 50 ml of 20 ppm MB aqueous solution and the mixture was stirred for 3 hours. As shown in Figure 11a under dark conditions, catalysts **ZnO/C-Ar₈₀₀**, **ZnO/C-Ar+W(S)₈₀₀** and **ZnO/C-Ar+W(L)₈₀₀** demonstrate substantial amount of dye adsorption up to 28, 53 and 34 % respectively. On the contrary, **ZnO-Air₈₀₀** exhibits almost no adsorption. The samples **C-Ar₁₀₀₀**, **ZnO/C-Ar+W(S)₁₀₀₀** and **ZnO/C-Ar+W(L)₁₀₀₀** (Figure 11c) adsorb 79, 89 and 86 % of the dye under dark room conditions respectively, but **ZnO-Air₁₀₀₀** shows no adsorption. Moreover, most of MB was adsorbed on the surface of the porous composites in the first 30 to 60 minutes before achieving an adsorption/desorption equilibrium. Obviously, the observed high degradation of MB in dark room conditions is mainly due to the high textural properties of the as-synthesized ZnO/C composites, which is consistent with our previous report.[27] To measure the photocatalytic performance of the composites, the photodegradation of MB was carried out under visible light irradiation. While sample **ZnO-Air₈₀₀** displayed 25% of MB photodegradation in 3 hours, samples **ZnO/C-Ar₈₀₀**, **ZnO/C-Ar+W(S)₈₀₀** and **ZnO/C-Ar+W(L)₈₀₀** showed adsorption and

photodegradation of 82, 99 and 92 %, respectively (Figure 11b). Compared with sample **ZnO-Air$_{800}$**, sample **ZnO-Air$_{1000}$** only showed 7.5 % photodegradation capacity under visible light irradiation, maybe due to the formation of large ZnO particles at higher heat process temperature. However, Figure 11d shows that the composites **C-Ar$_{1000}$**, **ZnO/C-Ar+W(S)$_{1000}$** and **ZnO/C-Ar+W(L)$_{1000}$** exhibited 80, 99 and 85 % of adsorption and photocatalytic degeneration of MB respectively. Comparing the photocatalytic activity of best performing composites **ZnO/C-Ar+W(S)$_{800}$** and **ZnO/C-Ar+W(S)$_{1000}$** under dark and visible light, it can be clearly observed that the photodegradation of MB is more dominant in **ZnO/C-Ar+W(S)$_{800}$** due to high content of ZnO whereas adsorption is more dominant in **ZnO/C-Ar+W(S)$_{1000}$** due to high content of carbon. In UV-vis absorption spectra, it is difficult to differentiate between simultaneous adsorption and photodegradation. It is evident that under the most suitable synthesis conditions the composites **ZnO/C-Ar+W(S)$_{800}$** and **ZnO/C-Ar+W(S)$_{1000}$** with homogeneously dispersed and carbon doped ZnO nanoparticles in the highly porous amorphous carbon framework show the best adsorption and photodegradation performance. Apparently, high surface area composite should show highest adsorption. However, these samples have not demonstrated best adsorption and dye degradation of MB. Confirmed by various characterization techniques (i.e. XRD, HRTEM, Raman spectroscopy, XPS and FTIR) not only surface areas but other parameters also play crucial role in adsorption and dye photodegradation. The presence of carboxylate (-COOH) functional groups and oxygen species on the surface of the catalysts provides active sites that increase the hydrophilic behavior and facilitates the MB molecules to be accommodated inside the pores and subsequently degraded, which consequently result in higher photocatalytic performance of composites derived from water vapor atmosphere than the ones prepared in argon atmosphere. It can be inferred that the porous framework, the hydrophilic functional groups on the surface of porous carbons, carbon doping and the homogeneous dispersion of ZnO nanoparticles play a significant role for the enhancement of adsorption and photocatalytic performance for dye degradation.
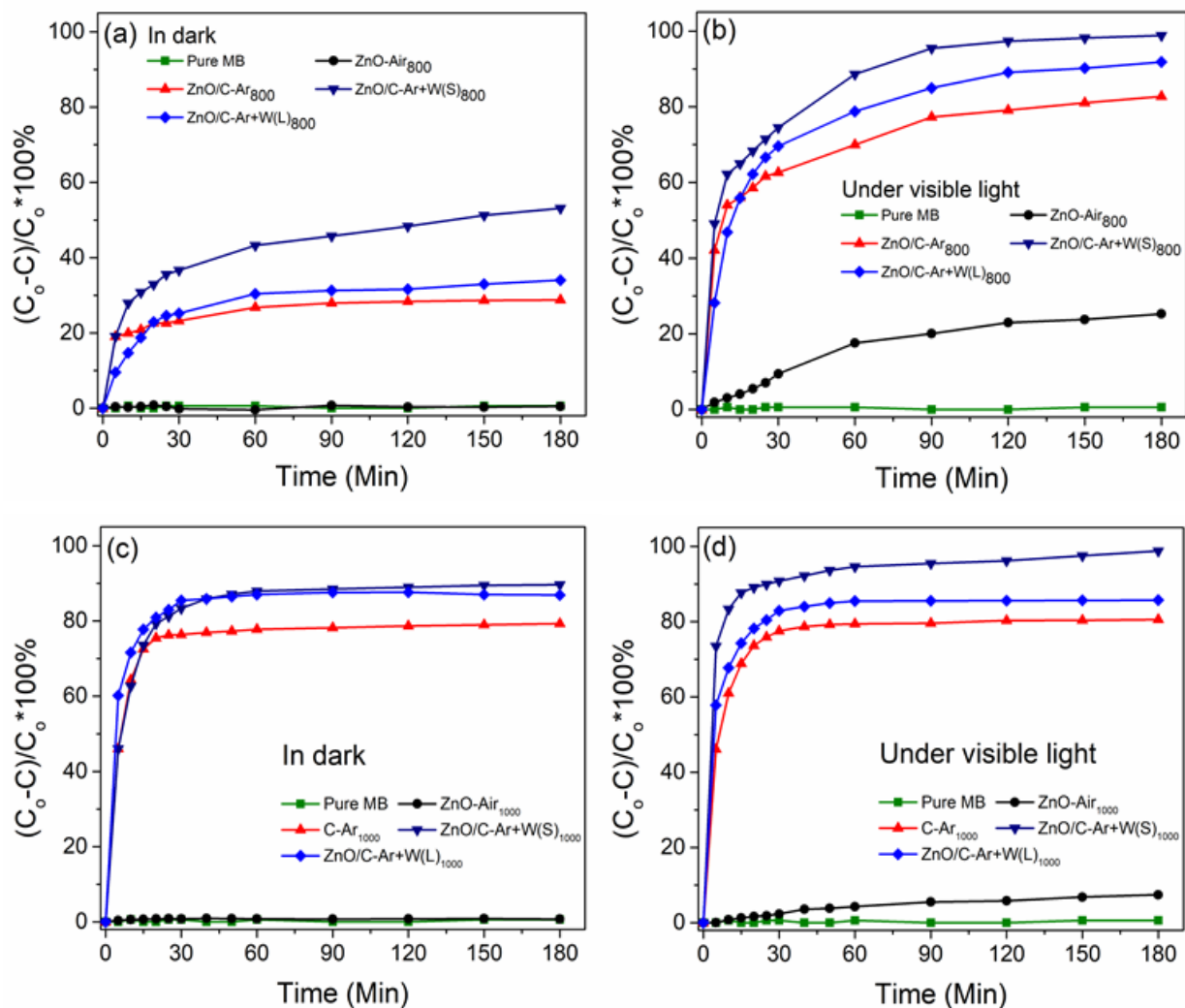
Figure 11. The adsorption and photodegradation of MB by **ZnO-Air** (black circles), **ZnO/C-Ar**(red triangles), **ZnO/C-Ar+W(L)** (light blue diamonds) and **ZnO/C-Ar+W(S)** (dark blue triangles) derived at 800 °C and 1000 °C in dark (a, c) and under visible light irradiation (b, d) respectively. Green squares represent blind test without any catalysts.

It has been reported that the decolorization of organic dyes could take place due to a self-sensitization mechanism.[1] Organic dyes show light absorption in visible light region, therefore the charge excitation takes place in the organic dye molecules, resulting in the formation of unstable cation radicals on the surface of the ZnO semiconductor. These generated active species attack the dye molecules leading to the decolorization of the dye without mineralization. The newly produced secondary products could be toxic. This mechanism can prevent the completely

24

mineralization of the organic dye into neutral species such as CO_2 and H_2O by actual photocatalysis.[1]

To confirm that the MB was completely neutralized by photocatalytic degradation, 25 mL of pure MB was placed under the visible light for 3 hours and the intensity of the absorption peaks was recorded by UV-vis spectrophotometry. There was no change in intensity of the MB for 3 hours which verified that the MB did not self-sensitize as shown in Figure 11a-d.
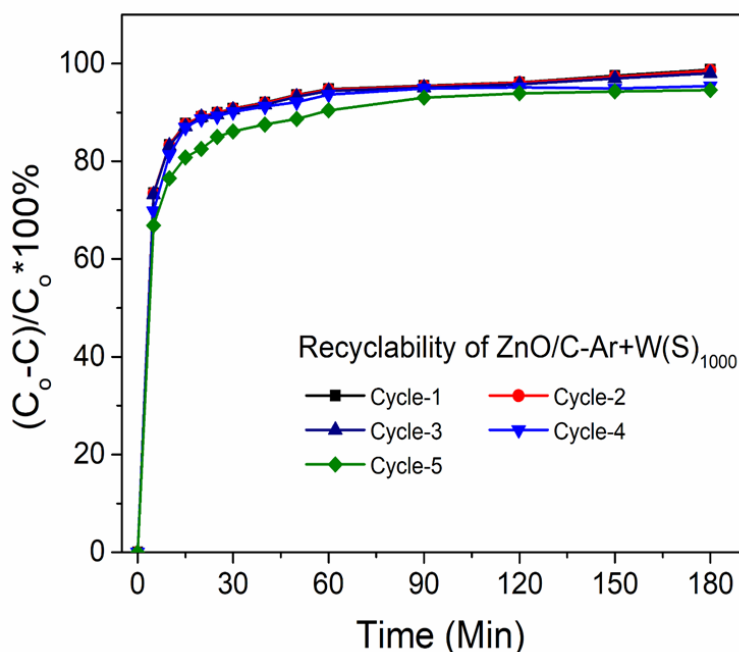

Figure 12. Recyclability test of the composite **ZnO/C-Ar+W(S)₁₀₀₀** for the adsorption and photodegradation of MB in water under visible-light irradiation.

To study the stability and reusability of the composites, **ZnO/C-Ar+W(S)₁₀₀₀** was tested in 5 consecutive MB degradation cycles. For this reusability test, 30 mg of the catalyst was put into 150 mL of 20 ppm MB solution and stirred for 3 hours. After each cycle, the used catalyst was filtered from the solution, washed several times with deionized water and dried over night at 110 °C before using for the next run. Figure 12 shows that the nanocomposite retains the efficiency over the whole five cycles with only negligible decreases. The 5th cycle showed still 94% photodegradation, signifying a good stability and reusability of the **ZnO/C-Ar+W(S)₁₀₀₀** nanocomposite. It can be established that the MOF derived ZnO/C nanocomposites do not form

25

bonds with water molecules and the microporous structure of composite remains intact, preventing the agglomeration of ZnO nanoparticles. In addition, the UV-vis absorption spectra were shown in Figure S7 confirmed that the absorption intensity decreases with time during the photocatalytic process. The MB absorbance remains at the same wavelength which indicates that no secondary products were formed due to the decolorization of the dye molecules. Eventually MB dye molecules are completely mineralized and led to the completely removal of MB from water, accompanied with the change of color from blue to colourless (as shown in Figure S8).

4. CONCLUSIONS

We have successfully synthesized ZnO/C nanocomposites by a simple one-step high temperature heat treatment of MOF-5 in different carbonization atmospheres. The ZnO/C composites with different carbon/metal oxide ratios are formed when derived at 800 °C and 1000 °C in air, argon and water vapor atmospheres respectively. After the carbonization process the inherent porosity and cubic structure of precursor MOF-5 remain in the resulting composites. All the composites demonstrate high photocatalytic activity compared to the pure ZnO nanoparticles obtained by heat treatment of MOF-5 in air. The composite derived at 1000 °C in argon saturated with water vapors for a short duration (1 h) outperforms all the other composites regarding the photocatalytic MB degradation. Defects in the crystalline structure of carbon doped ZnO and the presence of oxygen-containing hydrophilic -COOH functional groups on the surface of the composite functioned as traps for dye molecules and facilitate their photodegradation. The present study provides a simple and promising approach for the synthesis and application of homogeneously dispersed porous ZnO/C composites with excellent photocatalytic performance for the removal of organic pollutants from water.

ASSOCIATED CONTENT

Supporting Information

Supplementary data related to this article can be found in file attached.

ACKNOWLEDGEMENTS

Present Addresses

c Sandia National Laboratories, Livermore, CA 94551-0696 (USA)

REFERENCES

(1) Rochkind M.; Pasternak S.; Paz. Y. Using Dyes for Evaluating Photocatalytic Properties: A Critical Review. *Molecules* **2015**, *20*, 88-110.

(2) Kubacka A.; Fernandez-Garcia M.; Colon G. Advanced Nanoarchitectures for Solar Photocatalytic Applications. *Chem. Rev.* **2011**, *112*, 1555-1614.

(3) Galian R. E.; Perez-Prieto P. Catalytic Processes Activated by Light. *Energy Environ. Sci.*, **2010**, *3*, 1488-1498.

(4) Wang J.; Wang Z.; Huang B.; Ma Y.; Liu Y.; Qin X.; Zhang X.; Dai Y. Oxygen Vacancy Induced Band-Gap Narrowing and Enhanced Visible Light Photocatalytic Activity of ZnO. *Appl. Mater. Interfaces* **2012**, *4*, 4024-430.

(5) Liu S.; Li C.; Yu J.; Xiang Q. Improved Visible-Light Photocatalytic Activity of Porous Carbon Self-Doped Zno Nanosheet-Assembled Flowers**.** *CrystEngComm.* **2011**, *13***,** 2533-2541.

(6) Cho S.; Jang J.; Lee J.; Lee K., Carbon-Doped Zno Nanostructures Synthesized Using Vitamin C for Visible Light Photocatalysis. *CrystEngComm.* **2010**, *12*, 3929-3935.

(7) Alshammari A. S.; Chi L.; Chen X.; Bagabas A.; Kramer D.; Alromaeha A.; Jiang Z. Visible-Light Photocatalysis on C-Doped ZnO Derived from Polymer-Assisted Pyrolysis. *RSC Adv.* **2015**, *5*, 27690-27698.

(8) Oar-Arteta L.; Wezendonk T.; Sun X.; Kapteijn F.; Gascon J. Metal Organic Frameworks as Precursors for the Manufacture of Advanced Catalytic Materials. *Mater. Chem. Front.* **2017**, *1*, 1709-1745.

(9) Yang S. J.; Nam S.; Kim T.; Im J. H.; Jung H.; Kang J. H.; Wi S.; Park B.; Park C. R. Preparation and Exceptional Lithium Anodic Performance of Porous Carbon-Coated ZnO Quantum Dots Derived from a Metal–Organic Framework. *J. Am. Chem. Soc.* **2013**, *135*, 7394-7397.

(10) Pan L.; Muhammad T.; Ma L.; Huang Z.; Wang S.; Wang L.; Zou J.; Zhang X. MOF-Derived C-Doped ZnO Prepared via a Two-Step Calcination for Efficient Photocatalysis. *Appl. Catal. B: Environ.* **2016**, *189*, 181-191.

(11) Sun J.; Xu Q. Functional Materials Derived from Open Framework Templates/Precursors: Synthesis and Applications. *Energy Environ. Sci.* **2014**, *7*, 2071-2100.

(12) Tranchemontagne D. J.; Hunt J. R.; Yaghi O. M. Room Temperature Synthesis of Metal-Organic Frameworks: MOF-5, MOF-74, MOF-177, MOF-199, and IRMOF-0. *Tetrahedron* **2008**, *64*, 8553-8557.

(13) Yaghi O. M.; O'Keeffe M.; Ockwig N. W.; Chae H. K.; Eddaoudi M.; Kim J. Reticular Synthesis and the Design of New Materials. *Nature* **2003**, *423*, 705-714.

(14) Li H.; Eddaoudi M.; O'Keeffe M.; Yaghi O. M. Design and Synthesis of an Exceptionally Stable and Highly Porous Metal-Organic Framework. *Nature* **1999**, *402*, 276-279.

(15) Wu H.; Gong Q.; Olson D. H.; Li J. Commensurate Adsorption of Hydrocarbons and Alcohols in Microporous Metal Organic Frameworks. *Chem. Rev.* **2012**, *112*, 836-868.

(16) Banerjee R.; Furukawa H.; Britt D.; Knobler C.; O'Keeffe M.; Yaghi O. M. Control of Pore Size and Functionality in Isoreticular Zeolitic Imidazolate Frameworks and their Carbon Dioxide Selective Capture Properties. *J. Am. Chem. Soc.* **2009**, *131*, 3875-3877.

(17) Horcajada P.; Gref R.; Baati T.; Allan P. K.; Maurin G.; Couvreur P.; Ferey G.; Morris R. E.; Serre C. Metal–Organic Frameworks in Biomedicine. *Chem. Rev.* **2012**, *112*, 1232-1268.

(18) Sheberla D.; Bachman J. C.; Elias J. S.; Sun C.; Shao-Horn Y.; Dincă M. Conductive MOF Electrodes for Stable Supercapacitors with High Areal Capacitance. *Nature Mater.* **2017**, *16***,** 220-224.

(19) Demir-Cakan R.; Morcrette M.; Nouar F.; Davoisne C.; Devic T.; Gonbeau D.; Dominko R.; Serre C.; F´erey G.; Tarascon J. M. Cathode Composites for Li–S Batteries via the Use of Oxygenated Porous Architectures. *J. Am. Chem. Soc.* **2011**, *133*, 16154-16160.

(20) Yoon M.; Srirambalaji R.; Kim K. Homochiral Metal–Organic Frameworks for Asymmetric Heterogeneous Catalysis. *Chem. Rev.* **2012**, *112*, 1196-1231.

(21) Kreissl H. T.; Li M. M. J.; Peng Y.; Nakagawa K.; Hooper T. J. N.; Hanna J. V.; Shepherd A.; Wu T.; Soo Y.; Tsang S. C. E. Structural Studies of Bulk to Nanosize Niobium Oxides with Correlation to Their Acidity. *J. Am. Chem. Soc.* **2017**, *139*, 12670-12680.

(22) Kaye S. S.; Dailly A.; Yaghi O. M.; Long J. R. Impact of Preparation and Handling on the Hydrogen Storage Properties of $Zn_4O(1,4\text{-benzenedicarboxylate})_3$ (MOF-5). *J. Am. Chem. Soc.* **2007**, *129*, 14176-14177.

(23) Xie Z.; Xu w.; Cui X.; Wang Y. Recent Progress in Metal-Organic Frameworks and Their Derived Nanostructures for Energy and Environmental Applications. *ChemSusChem* **2017**, *10*, 1645-1663.

(24) Chen Y.; Zhang R.; Jiao L.; Jiang H. Metal–Organic Framework-Derived Porous Materials for Catalysis. *Coord. Chem. Rev.* **2018**, *362*, 1–23

(25) Teng W.; Bai N.; Chen Z.; Shi J.; Fan J.; Zhang W. Hierarchically Porous Carbon Derived from Metal-Organic Frameworks for Separation of Aromatic Pollutants. *Chem. Eng. J.* **2018**, *346*, 388-396.

(26) Yang S. J.; Im J. H.; Kim T.; Lee K.; Park C. R. MOF-Derived ZnO and Zno@C Composites with High Photocatalytic Activity and Adsorption Capacity. *J. Hazard. Mater.* **2011**, *186*, 376-382.

(27) Chen B.; Ma G.; Kong D.; Zhu Y.; Y. Xia Y. Atomically Homogeneous Dispersed ZnO/N-Doped Nanoporous Carbon Composites with Enhanced CO_2 Uptake Capacities and High Efficient Organic Pollutants Removal from Water. *Carbon* **2015**, *95*, 113-124.

(28) Ma M.; Zacher D.; Zhang X.; Fischer R. A.; Metzler-Nolte N. A Method for the Preparation of Highly Porous, Nanosized Crystals of Isoreticular Metal−Organic Frameworks. *Cryst. Growth DesigN* **2011**, *11*, 185-189.

(29) Huang L.; Wang H.; Chen J.; Wang Z.; Sun J.; Zhao D.; Yan Y. Synthesis, Morphology Control, and Properties of Porous Metal–Organic Coordination Polymers. *Micropor. Mesopor. Mater.* **2003**, *58*, 105-114.

(30) Abbasi Z.; Shamsaei E.; Leong S. K.; Ladewig B.; Zhang X.; Wang H. Effect of Carbonization Temperature on Adsorption Property of ZIF-8 Derived Nanoporous Carbon for Water Treatment. *Micropor. Mesopor. Mater.* **2016**, *236*, 28-37.

(31) Hafizovic J.; Bjørgen M.; Olsbye U.; Dietzel P. D. C.; Bordiga S.; Prestipino C.; Lamberti C.; Lillerud K. P. The Inconsistency in Adsorption Properties and Powder XRD Data of MOF-5 is Rationalized by Framework Interpenetration and the Presence of Organic and Inorganic Species in the Nanocavities. *J. Am. Chem. Soc.* **2007**, *129*, 3612-3620.

(32) Nesakumar N.; Rayappan J. B. B.; Gopalakrishnan B.; Prakash J.; Krishnan U. M. Influence of pH on Structural Morphology of ZnO Nanoparticle. *J. Appl.Sci.* **2012**, *12*, 1758-1768.

(33) Torad N. L.; Hu M.; Ishihara S.; Sukegawa H.; Belik A. A.; Imura M.; Ariga K.; Sakka Y.; Yamauchi Y. Direct Synthesis of MOF-derived Nanoporous Carbon With Magnetic Co Nanoparticles Toward Efficient Water Treatment. *Small* **2014**, *10*, 2096-2107.

(34) Srinivas G.; Krungleviciute V.; Guo Z.; T. Yildirim T. Exceptional CO_2 Capture in A Hierarchically Porous Carbon With Simultaneous High Surface Area and Pore Volume. *Energy Environ. Sci.* **2014**, *7*, 335-342.

(35) Han M.; Yin X.; Ren S.; Duan W.; Zhang L.; Cheng L. Core/shell Structured C/ZnO Nanoparticles Composites for Effective Electromagnetic Wave Absorption. *RSC Adv.* **2016**, *6*, 6467-6474.

(36) Özgür Ü.; Alivov Y. I.; Liu C.; Teke A.; Reshchikov M. A.; Doğan S.; Avrutin V.; Cho S.-J.; Morkoç H. A Comprehensive Review of ZnO Materials and Devices. *J. Appl. Phys.* **2005**, *98*, 041301.

(37) Son D. I.; Kwon B. W.; Park D. H.; Seo W.; Yi Y.; Angadi B.; Lee C.; Choi W. K. Emissive ZnO–graphene Quantum Dots for White-Light-Emitting Diodes. *Nature Nanotechno.* **2012**, *7*, 465-471.

(38) Cuscó R.; Alarcón-Lladó E.; Ibáñez J.; Artus L.; Jimenez J.; Wang B.; Callahan M. J. Temperature Dependence of Raman Scattering in ZnO. *Phys. Rev. B* **2007**, *75*, 165202.

(39) Chu P. K.; Li L. Characterization of Amorphous and Nanocrystalline Carbon Films. *Mater. Chem. Phys.* **2006**, *96*, 253-277.

(40) Ferrari A. C.; Robertson J. Interpretation of Raman Spectra of Disordered and Amorphous Carbon. *Phys. Rev. B* **2000**, *61*, 14095-14107.

(41) Dillon R. O.; Woollam J. A.; Katkanant V. Use of Raman Scattering to Investigate Disorder and Crystallite Formation in as-deposited and Annealed Carbon Films. *Phys. Rev. B* **1984**, *29*, 3482-3489.

(42) Tai F. C.; Lee S. C.; Wei C. H.; Tyan S. L. Correlation between ID/IG Ratio from Visible Raman Spectra and sp2/sp3 Ratio from XPS Spectra of Annealed Hydrogenated DLC Film. *Mater. Trans.* **2006**, *47*, 1847-1852.

(43) Thakur S.; Barua S.; Karak N. Reduced Graphene Oxide-Metal Oxide Nanohybrid for Efficient Adsorption, Photodegradation and Photoinactivation of Chemical and Microbial Contaminants. *J. Nanotech. Diagnosis Treatment* **2015**, *3*, 12-22.

(44) Mishra D.K.; Mohapatra J.; Sharma M. K.; Chattarjee R.; Singh S. K.; Varma S.; S.N. Behera S.N.; Nayak S. K.; Entel P. Carbon Doped ZnO: Synthesis, Characterization and Interpretation. *J. Magn. Magn. Mater.* **2013**, 329, 146–152.

(45) Yang S.; Zhi L.; Tang K.; Feng X. L.; Maier J.; Mullen K. Efficient Synthesis of Heteroatom (N or S)-Doped Graphene Based on Ultrathin Graphene Oxide-Porous Silica Sheets for Oxygen Reduction Reactions. *Adv. Funct. Mater.* **2012**, *22*, 3634-3641.

(46) Wang J.; Zhong H. X.; Qin Y. L.; Zhang X. B. An Efficient Three-Dimensional Oxygen Evolution Electrode. *Angew. Chem. Int. Ed.* **2013**, *52*, 5248-5253.

(47) Ferrari A. C. Raman Spectroscopy of Graphene and Graphite: Disorder, Electron–Phonon Coupling, Doping and Nonadiabatic Effects. *Solid State Commun.* **2007**, *143*, 1-2, 47-57.

(48) Liang P.; Zhang C.; Sun H.; Liu S.; Tade M.; Wang S. Solar Photocatalytic Water Oxidation and Purification on ZIF-8-Derived C–N–ZnO Composites. *Energy Fuels* **2017**, *31*, 2138-2143.